Hindawi
Geofluids
Volume 2021, Article ID 9988120, 21 pages
https://doi.org/10.1155/2021/9988120

Research Article

Numerical Study on the Mechanism and Application of Artificial Free Surfaces in Bedrock Blasting of Shield Tunnels

Yanjun Qi,[1,2] **Linming Dou**,[2] **Zhaoxing Dong**,[1] **Zheng Jiang**,[1] **Bo Meng**,[1] **and Junzhong Zhang**[1]

[1]*School of Mechanics and Civil Engineering, China University of Mining and Technology, Xuzhou 221116, China*
[2]*State Key Laboratory of Coal Resources and Safe Mining, China University of Mining and Technology, Xuzhou 221116, China*

Correspondence should be addressed to Linming Dou; lmdou@126.com

Received 23 March 2021; Revised 7 April 2021; Accepted 13 April 2021; Published 3 May 2021

Academic Editor: Yu Wang

During the pretreatment construction of blasting in shield tunnel bedrock, in order to reduce the impact of blasting vibration on the surrounding environment and improve the effect of rock blasting, the method of creating an artificial free surface is proposed. From the point of creating an artificial free surface, this paper numerically studies the function mechanism and parameter optimization of artificial free faces in shield tunnel bedrock blasting construction. The propagation characteristics of explosion stress waves at the interface between the rock and the artificial free face and the effect of the artificial free face on the shield tunnel bedrock blasting were analyzed. The results indicate that, as the explosion stress wave transmits to the artificial free face, a part of the stress wave is reflected back to the bedrock, increasing the energy in the bedrock that needs blasting and improving the blasting effect and utilization rate of the blasting energy. The reduction degree of the peak velocity of the surface particle is more than 50%, and the reduction degree of the peak velocity of the particle near the artificial free face is more than 77%. The existence of the artificial free face reflects the stress wave and superimposes with the original stress waves, increasing the effective stress in the blasting area, and the effective stress can be increased by 5 MPa or more. The peak vibration velocity of the surface particle decreases with an increasing diameter of the empty holes and the distance between the empty holes and the blasting holes. The parameter design value of the artificial free face is put forward: the diameter of the hole is 200 mm, the distance between the empty holes and the center of the blasting holes is 60 cm, and the depth of the empty hole is the same as the blasting hole.

1. Introduction

With the continuous improvement of the urbanization level, urban transportation construction has developed rapidly, gradually developing in a multilevel and three-dimensional direction [1, 2]. Among them, the subway has been developed vigorously because it can effectively relieve the traffic pressure and reduce the road mileage to a certain place. The subway has become the main project of urban transportation construction [3]. Subway projects are characterized by long lines, variable geological conditions, and complex surrounding environments [4, 5], and along with the maturing of the shield construction technology, more and more subway projects adopt shield construction to improve the construction efficiency and safety of subway projects [6]. Boulder groups and bedrock intrusion are the most representative cases in composite strata. This kind of rock mass is usually granite, and its strength is far greater than the strongly weathered surrounding rock mass, resulting in great security risks to shield engineering, which needs to be pretreated [7]. For the treatment of this situation, the blasting pretreatment technology of "ground drilling, millisecond blasting in the hole" is mainly used. Before the shield construction, a geological drilling machine is used to drill a hole vertically on the ground. A special charge is made to pretreat the boulder or bedrock intrusion in the composite stratum by

Figure 1: Rock sample preparation and the testing system.

blasting. The blasting pretreatment technology meets the requirements of the fragmentation in shield tunneling, which largely solves the difficulties encountered in shield construction and promotes the development of tunnel construction [8–11].

In actual engineering blasting, the vibration induced by the blast of the explosive is always a problem [12–15]; it can damage the buildings near the blasting resources [16, 17]. The artificial free surface is one of the important factors that affect the blasting effect, which has been widely studied by scholars all over the world [18–20]. In Ref. [21], it was found that empty holes between the blasting holes can control the expansion direction of the blasting lines. In Ref. [22], the authors investigated the influence of different intervals between blasting holes on crack propagation with a dynamic caustic test and numerical simulation. With the increase of intervals between the holes, the explosion cracks show no direct penetration anymore; rather, the deflection of cracks occurs in a "hand in hand" shape. In Ref. [23], the authors conducted a numerical study on deep-hole blasting and found that the explosion gas pressure has a significant impact on the formation and development of cracks in deep rocks without free faces. In Ref. [24], the authors found that a satisfactory blasting effect could be obtained when a free face exists and blasting efficiency could be improved to a large extent through field tests. In Ref. [25], the authors found that the existence of a free face could effectively improve the utilization rate of the explosion energy by studying the model test of single-hole blasting. In Ref. [26], the author believes that the charging hole should be as close to the free face as possible. If the free face is not flat and parallel to the gun hole, the effective utilization of the explosion energy can be improved, and similarly, the blasting effect can also be improved. Through numerical analysis, it was found that the free face has a strong control effect on the blasting vibration near it [27]. According to a similar law obtained in Ref. [28], the distance between the blasting source and the free face has a certain influence on the vibration velocity of the surface particles.

These previous researches provide good theoretical basis and research methods for the study of the mechanisms of an artificial free face in shield tunnel bedrock blasting. However, at present, the research on the mechanism of a rock burst mainly focuses on the construction of tunnel blasting and excavation. Research on the pretreatment technology of rock blasting in shield tunnels is still in its infancy. Besides, research on free faces mainly focuses on existing surfaces, and research on the action mechanisms of an artificial free face is relatively scarce. As the buildings around the blasting area become denser and the construction conditions become more complicated, the artificial free face will play an important role in any future construction.

Table 1: Uniaxial compressive strength and axial strain of granites.

Sample no.	UCS (MPa)	Average UCS (MPa)	Axial failure strain	Average axial failure strain
DY1	117.21	114.01	0.0053	0.0055
DY2	112.41		0.0057	
DY3	123.67		0.0061	
DY4	102.72		0.0048	

This article takes the blasting construction of the shield tunnel in the Binhu section at Line 6 of the Fuzhou Metro as the engineering background to numerically analyze the propagation characteristics of the explosion stress waves in the rock mass and the effect of the artificial free face on the blasting of the shield tunnel bedrock. According to the actual engineering background, a series of numerical simulations were carried out to reveal the function mechanisms of the artificial free faces in the shield tunnel bedrock blasting, and the simulation results with and without a free face were compared. Then, based on the data and rules, the parameters of the artificial free face are studied, including the diameter of the empty holes and the distance between the empty holes and the blasting holes. The influence of different parameters on the effect of controlling the artificial free face is investigated. Finally, parameter optimization of the artificial free face was conducted.

2. Testing and Analysis of the Mechanical Properties of Granite

During the construction process of shield tunnel bedrock blasting pretreatment, the target objects are the bedrock and solitary stone groups in the stratum where the granite is the main lithology. There are dynamic loads such as explosion and shock impacts on granites in the process of ground drilling, bedrock blasting, and explosion stress wave propagation. Therefore, it is necessary to understand the mechanical properties of granites to fully grasp the fracture mechanism of granite under impact load and the stress wave propagation law to provide corresponding parameters for the numerical simulation.

Table 2: Deformation characteristics of granite samples.

Sample no.	Secant Young's modulus (MPa)		Tangent elasticity modulus (MPa)		Poisson's ratio	
	Single value	Average value	Single value	Average value	Single value	Average value
DY1	19493.8	18959.6	25023.9	24713.3	0.26	0.26
DY2	17478.5		26075.2		0.25	
DY3	17698.4		26302.5		0.31	
DY4	21167.7		21451.6		0.21	

Figure 2: Failure patterns of granite samples after uniaxial compression tests.

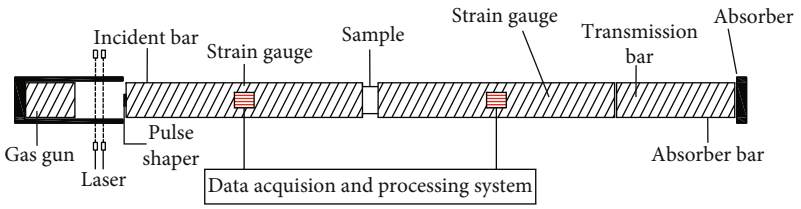

Figure 3: The SHPB testing system.

2.1. Uniaxial Compressive Results of Granites. The rock samples used in this paper were obtained from field drilling in the Binhu section at Line 6 of the Fuzhou Metro. Samples with relatively good integrity and homogeneity were selected. According to the suggested method of the International Society of Rock Mechanics (ISRM), uniaxial compression tests were conducted on granite samples with a diameter of 50 mm and a height of 100 mm (length diameter ratio of 2.0), and Split Hopkinson Pressure Bar (SHPB) tests were conducted on samples with a diameter of 50 mm and a height of 25 mm (length diameter ratio of 0.5). The error of nonparallelism and nonperpendicularity of the end surfaces for the samples should be controlled within 0.02 mm. Through the process of coring, cutting, and grinding, the rock samples were prepared, as shown in Figure 1.

Before the experiment, the prepared granite samples were first inspected, and the samples, which were smooth and flat, with parallelism, straightness, and perpendicularity all meeting the requirements, and with no obvious joints, cracks, and other defects, were finally selected. The uniaxial compression tests were conducted using the MTS-815 electrohydraulic servo rock testing system (Figure 1). The experimental

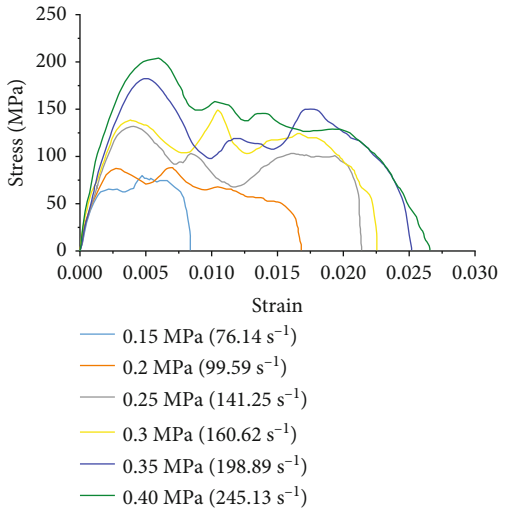

Figure 4: Stress-strain curves in the SHPB tests.

Table 3: Results of uniaxial impact compression tests of granites.

Excitation pressure (MPa)	Sample no.	Average strain rate (s^{-1})		Peak stress (MPa)		Peak strain	
		Single value	The average	Single value	The average	Single value	The average
	A-1	80.991		70.974		0.0021	
	A-2	63.173		68.236		0.0032	
0.15	A-3	83.269	76.137	60.498	64.78	0.0018	0.0023
	A-4	82.367		58.867		0.0025	
	A-5	70.236		65.324		0.0017	
	B-1	115.596		99.497		0.0031	
	B-2	135.123		91.573		0.003	
0.2	B-3	110.829	99.594	75.323	89.685	0.0026	0.003
	B-4	131.671		89.989		0.0025	
	B-5	120.346		92.043		0.0035	
	C-1	142.131		130.748		0.0041	
	C-2	152.041		140.079		0.0039	
0.25	C-3	144.572	141.25	144.217	141.055	0.0046	0.0042
	C-4	138.201		149.461		0.0035	
	C-5	129.311		140.771		0.0049	
	D-1	159.509		166.638		0.0049	
	D-2	175.639		176.693		0.0051	
0.3	D-3	160.438	160.62	138.864	158.961	0.0046	0.0053
	D-4	158.268		152.368		0.0057	
	D-5	149.235		160.235		0.0062	
	E-1	203.609		157.269		0.0058	
	E-2	196.089		201.446		0.0065	
0.35	E-3	207.223	198.9	183.247	178.105	0.0063	0.0062
	E-4	189.324		170.236		0.0057	
	E-5	198.235		178.327		0.0067	
	F-1	251.935		200.583		0.0091	
	F-2	247.507		215.491		0.0078	
0.4	F-3	237.496	245.13	193.679	203.599	0.0073	0.0083
	F-4	226.157		208.623		0.0083	
	F-5	262.548		199.623		0.0087	

results, including the uniaxial compressive strength (UCS), axial failure strain, secant Young's modulus, tangent elasticity modulus, and Poisson's ratio are, respectively, listed in Tables 1 and 2. The average UCS is 114.01 MPa, and the average axial failure strain is 0.0055. The average secant Young's modulus and average tangent elasticity modulus are 18959.6 MPa and 24713.3 MPa, respectively, with the average Poisson's ratio of 0.26. Ultimate failure modes of rock samples after uniaxial compression are displayed in Figure 2, which are characterized by typical splitting failure modes with tensile cracks along the loading direction.

2.2. Dynamic Mechanical Properties of Granites. The dynamic compression tests of granites were conducted using the SHPB device, which is composed of six units, including the dynamic system, bar system, supporting parts and guide rails, damper, velocimeter, and the data acquisition and processing systems, as shown in Figure 3. Due to the strain rate dependence and properties of the applied equipment, 6 sets

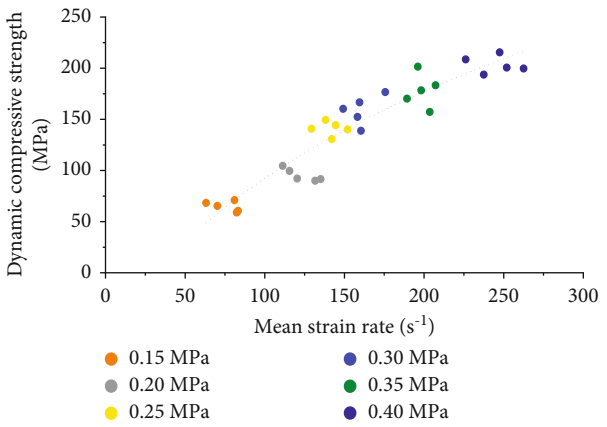

Figure 5: Relations between dynamic compressive strength and the average strain rate.

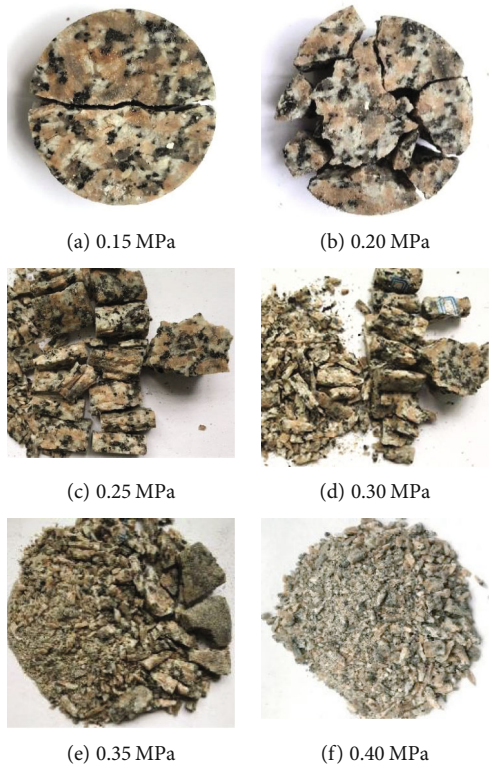

(a) 0.15 MPa (b) 0.20 MPa

(c) 0.25 MPa (d) 0.30 MPa

(e) 0.35 MPa (f) 0.40 MPa

Figure 6: Granite crushing degree and crushing form with various excitation pressures.

of impact compression tests with various excitation pressures of 0.15 MPa, 0.20 MPa, 0.25 MPa, 0.30 MPa, 0.35 MPa, and 0.40 MPa were, respectively, performed. Each set of tests was repeated for 5 times, with the stress-strain curves displayed in Figure 4.

From Figure 4, the shape of stress-strain curves under various impact loads is similar, which includes the following 4 steps: the initial compaction stage, the elastic deformation stage, the nonlinear deformation stage, and the failure stage. When the strain rate is low, the proportion of the initial compaction stage in the prepeak curves is larger, mainly because when the strain rate is low, there is less energy obtained by the sample and the initial microcrack closure is slower. With the increase of the strain rate, the proportion of the elastic stage in the prepeak curves gradually increases, more cracks are closed, and the closure speed is faster. After entering the nonlinear stage, the peak stress of the sample increases obviously, which shows that the granite has obvious strain rate characteristics under dynamic loads.

The average peak stress and peak strain under different impact loads of granite samples were calculated, as listed in Table 3.

Dynamic compressive strength and the strain rate are important parameters for analyzing the rock mechanical properties. According to the stress-strain time history curves, the relations between the two factors can be obtained, as shown in Figure 5.

Generally, the dynamic peak compressive strength of granites increases with the increase of the average strain rate.

Table 4: Classification of intervals of intrusion bedrock.

Classification of intrusive bedrock	Length (m)	Proportion
Small-volume bedrock	76	20.70%
Medium-volume bedrock	218	66.80%
Large-volume bedrock	40	12.50%

Curve fitting is performed to obtain the functional relationship between the two factors, as follows:

$$\begin{aligned} \sigma_d &= 118.61 \ln \dot{\varepsilon} - 450.32, \\ R^2 &= 0.9324. \end{aligned} \tag{1}$$

With the increase of the average strain rate, the dynamic compressive strength of granites gradually increases, indicating that the ultimate bearing capacity of granites increases correspondingly. However, at higher strain rates, the increased extent of the peak dynamic compressive strength gradually slows down.

After the dynamic compression tests, the ultimate failure modes of granites under different impact pressures are shown in Figure 6. Obviously, with an increasing excitation pressure, the fragmentation size of the sample decreases gradually and the number of fragments and the crushing degree increase gradually, indicating a strong strain rate effect.

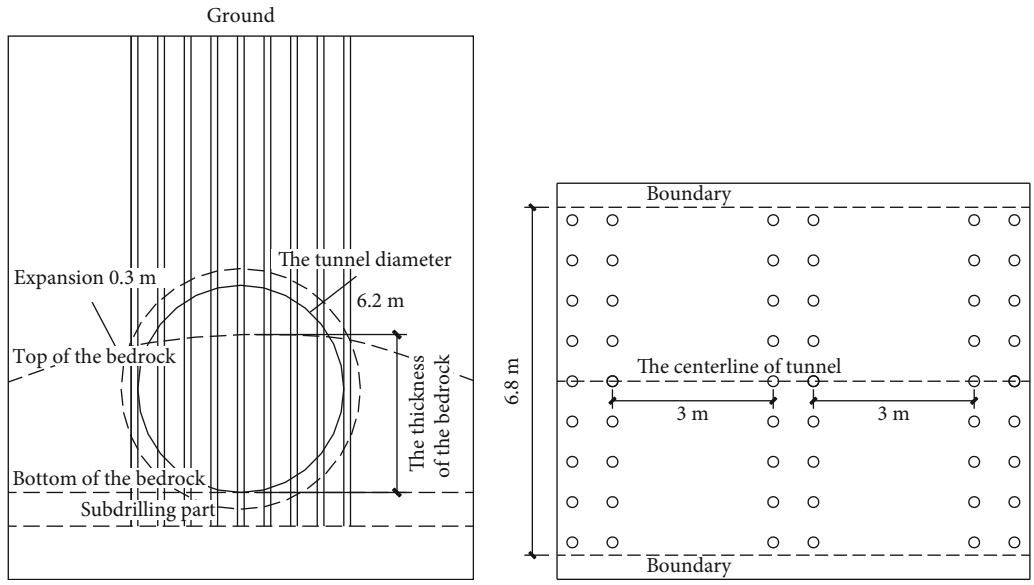

(a) Diagram of ultradeep drilling (b) Diagram of blasting zone

Figure 7: Layout diagram of the blasting holes.

Table 5: Bedrock blasting parameters.

Thickness of the bedrock (m)	Depth (m)	Pitch row (m)	Row spacing (m)	Hole depth (m)	Unit consumption (kg/m^3)	Charging mass (kg)	Charge structure
2	0.8	0.8	0.8	2.8	1.8	4.3	Continuous
3	1	0.8	0.8	4	1.9	7.6	Interval
5	1.5	0.8	0.8	6.5	2.1	10.3	Interval

3. Numerical Simulation of Bedrock Blasting in Shield Tunnels with Artificial Surfaces

3.1. Engineering Background. The Binhai Xincheng Station~-Hujing Station of Fuzhou Rail Transit Line 6, referred to as the Binhu interval, is taken as the engineering background. The shield tunneling method was used to construct the tunnel. The diameter of the interval shield tunnel is 6.2 m, and the tunnel is covered with soil with a thickness of about 8.51 m~15.21 m. Detailed survey data show that there are large areas of moderately weathered granites and slightly weathered granites along the shield line. The uplift of bedrock (soft rock on top and hard rock at the bottom) can easily cause damage to the main bearing and cutter head of the shield tunneling machine, producing serious effects on the process of shielding and resulting in ground subsidence beyond the tolerated limit and in eventual collapse.

The intruded bedrock in the section is classified according to the thickness of the intrusive rock (i.e., the distance between the top surface of the bedrock and the bottom surface of the tunnel). The bedrock thickness below 2 m is called the small-volume bedrock, the bedrock thickness between 2 m and 4 m is called the medium-volume bedrock, and the bedrock thickness between 4 m and 6 m is called the large-volume bedrock. The statistics of bedrock in the section are shown in Table 4, in which the medium-volume bedrock is the most prominent.

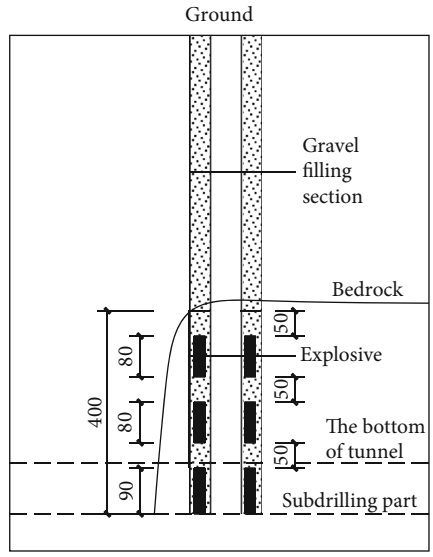

Figure 8: Schematic diagram of bedrock charge structures.

In order to ensure safe passage of the shield machine and meet the requirements of mucking out, it is necessary to blast

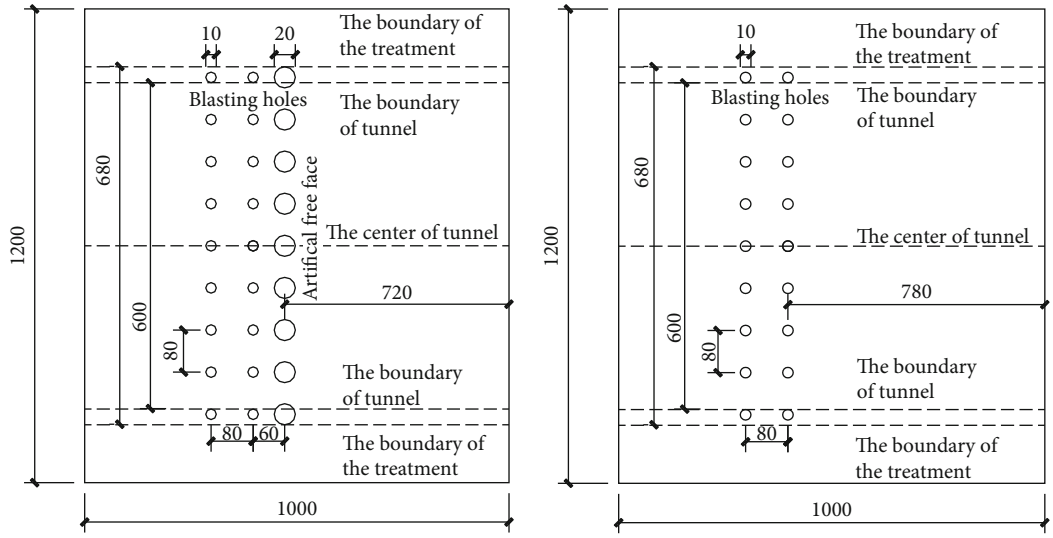

(a) With a free face (b) Without a free face

Figure 9: The numerical model plan (unit: cm).

the bedrock into fragments with a maximum length of less than 30 cm on one side. At the same time, it is also necessary to ensure that the buildings around the blasting area are not influenced by the construction. Combined with the corresponding provisions of the blasting safety regulations, the vibration velocity of the building foundation particles caused by the blasting pretreatment construction of the shield tunnel in the Binhu section should not be greater than 3 cm/s, and the vibration velocity of the building foundation particles directly above the right line should not be greater than 2.5 cm/s.

The diameter of the shield tunnel is 6.2 m, and both sides of the tunnel need to be expanded by 30 cm during the blasting treatment. The depth of the borehole is 0.8 m~1.5 m, and the charging depth is about 0.8 m~1 m deeper than the bottom of the tunnel. The blast holes are arranged in a rectangular layout, and the row spacing between the holes is 0.8 m × 0.8 m. Borehole blasting is carried out by blasting division, with 2 rows of blasting holes and an interval of about 3 m. The layout diagram of the blasting holes is shown in Figure 7. When the construction is near the building directly above the right line, it is necessary to add a row of empty holes near the charging hole at the side of the buildings to ensure the safety of the building structures.

According to actual construction experience, it is suggested that the shield machine should grind the rock directly when the bedrock thickness is more than 6 m. By calculating unit consumption, the charging parameters of different bedrock thicknesses are shown in Table 5.

It can be seen from Table 4 that the intrusive bedrock in the shield tunnel section is mainly medium-volume bedrock. Thus, the treatment depth of the bedrock is 4 m, as shown in Figure 8.

3.2. The Establishment of Model

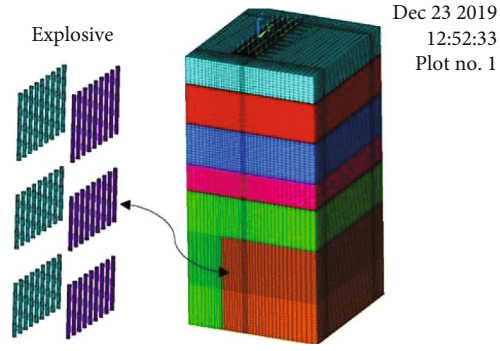

Figure 10: Bedrock blasting model.

3.2.1. Establishment of Numerical 3D Model. The main purpose of creating a free face is to reduce the damage caused by blasting vibration and improve the crushing effects of rock. According to actual construction experience, the artificial free holes should be arranged near the charging holes, and the artificial free face should be arranged on the side of the building that needs to be protected. In order to facilitate the actual construction, the empty holes are generally arranged in parallel with the charging holes, and the number of empty holes is the same as the number of charging holes. The diameter of the artificial empty holes should be larger than the diameter of the blast holes, and the distance between artificial empty holes and blast holes should be smaller than the row spacing of the blasting holes.

Combined with the engineering background of bedrock blasting pretreatment in the shield tunnel section, and considering the drilling diameter of the geological drill, the diameter of the artificial empty holes is selected as 200 mm, with the vertical distance from the blast holes of 60 cm. The depth of the empty hole is the same as the depth of the blasting hole. The numerical simulation includes two groups: one group

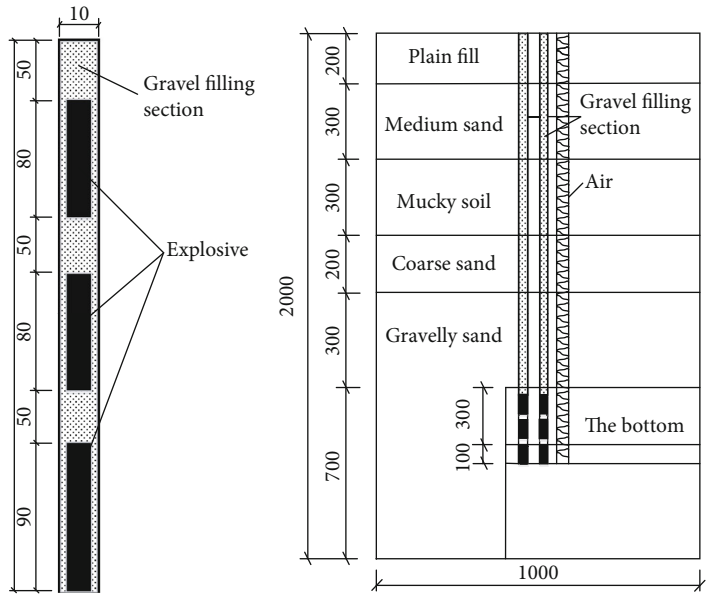

Figure 11: The vertical dimension and charging structures of the bedrock model.

Table 6: Explosive parameters.

Name	ρ (g/cm^3)	D (m/s)	P_{cj} (GPa)	A (GPa)	B (GPa)	R_1	R_2	ω	E (GPa)
Explosive	0.95	3400	5.3	162.7	10.82	5.4	1.8	0.25	4.1

Table 7: Material parameters of granites.

Rock types	Young's modulus E	Bulk modulus K	Shear modulus K_s	Lamme coefficient λ	Poisson's ratio λ_p	Density ρ
Granite	25 GPa	17 GPa	10 GPa	3.5	0.26	2.71 g/cm^3

with and the other group without artificial empty holes. The group with empty holes is taken as the control group, and the improvement of the blasting effect is obtained by analyzing the numerical results. The plan of the numerical model test is shown in Figure 9.

The software applied in this numerical simulation is LS-DYNA. According to the above engineering background and the diagram of bedrock explosion structures, a three-dimensional model of bedrock blasting is established, as shown in Figure 10. The vertical dimensions and charging structures of the bedrock model are shown in Figure 11.

According to Table 4, the medium-volume bedrocks were mainly distributed in this project, so medium-volume rocks were used as the bedrock in the simulation process. As shown in Figure 11, the thickness of bedrock intrusion into the tunnel is 3 m and the ultradeep drilling holes need to be 1 m below the tunnel bottom. Therefore, the actual thickness of the bedrock that needs to be treated is 4 m. Two rows of blasting holes are arranged according to the actual construction situation. The diameter of the shield tunnels is 6.2 m, and the actual treatment range is 6.8 m, based on the outward expansion of 30 cm on both sides. Nine blasting holes are set in each row, with a diameter of 100 mm and a spacing of 80 cm.

Table 8: Air parameters.

ρ (kg/m^3)	C_0	C_1	C_2	C_3	C_4	C_5	C_6	E_0	V_0
1.290	0	0	0	0	0.4	0.4	0	2.5×10^5	1

Table 9: Correlated parameters of the soil.

Name	ρ (cm^3)	E (MPa)	μ
Plain fill	1.8	20	0.26
Medium sand	2.05	37	0.25
Silty clay	1.95	15	0.35
Coarse sand	1.95	40	0.27
Gravelly sand	1.9	33	0.31

The arrangement of explosives is shown in Figure 11. The diameter of the charge is 60 mm. The uncoupled interval charge is adopted, and the initiation point is located at the 1/3 position above the bottom of the charge. When the bedrock thickness is 4 m, according to the blasting scheme, the charge is divided into three stages. The upper two explosive packages are 0.8 m, and the lower one is 0.9 m. The bedrock in the blasting interval near the buildings is located about

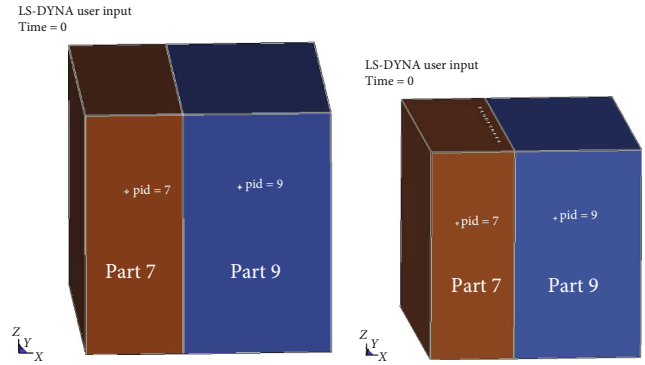

(a) Without an artificial free face (b) With an artificial free face

Figure 12: Bedrock model composition.

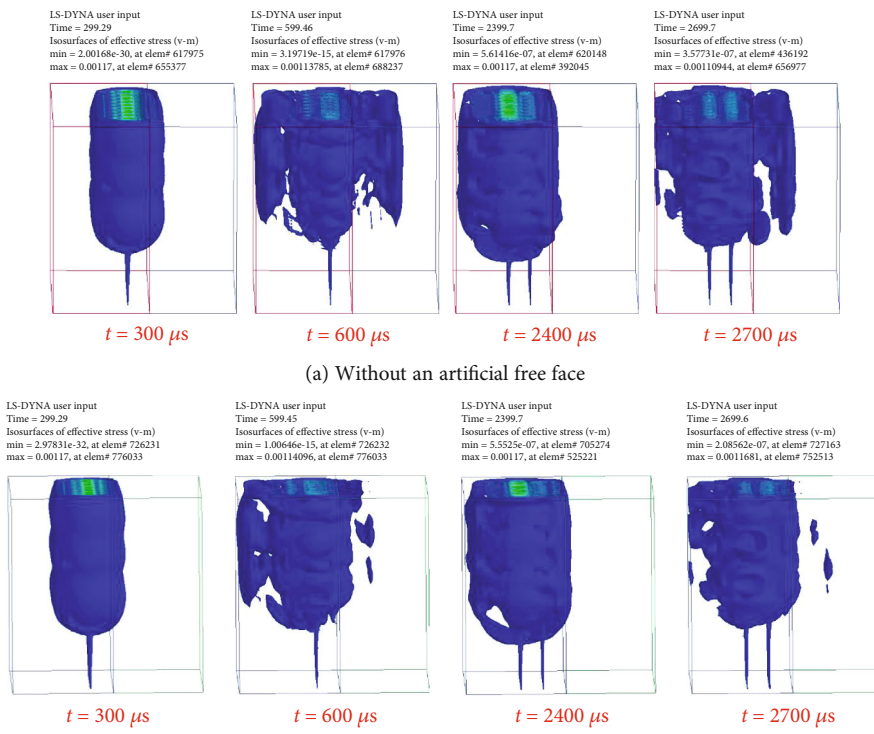

(a) Without an artificial free face

(b) With an artificial free face

Figure 13: Comparison of bedrock stress clouds.

13 m below the surface, so the established bedrock in the numerical model is located 13 m below the surface, with the model height, width, and length of 20 m, 10 m, and 12 m, respectively.

Considering that the size of the numerical model is limited to a certain extent, the nonreflection boundary is applied to all the five boundaries except the surface of the model to prevent the reflection of explosion stress waves at the model boundaries. In the numerical calculation, if the grid size is too large, the calculation accuracy will decline. If the grid is too dense, the calculation time will be prolonged and the calculation efficiency will be affected. Generally, the minimum size of the unit should be less than 1/10 of the wave length, so the maximum size of the grid in this model is 20 cm. At the same time, the explosive, bedrock, and air parts are refined and densified.

3.2.2. Constitutive Model and Parameter Selection. The explosive constitutive model provided by LS-DYNA was adopted, and the JWL state equation was used to simulate the detonation process of explosives, in the following form:

$$P = A\left(1 - \frac{\omega}{R_1 V}\right)e^{-R_1 V} + B\left(1 - \frac{\omega}{R_2 V}\right)e^{-R_2 V} + \frac{\omega E_0}{V}, \quad (2)$$

where P is pressure; V is the relative volume; E_0 is the initial

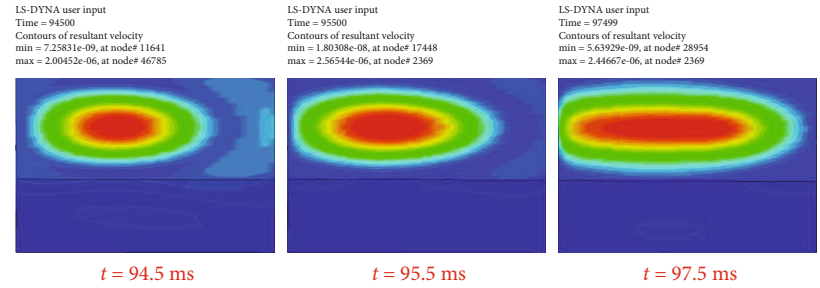

(a) Without an artificial free face

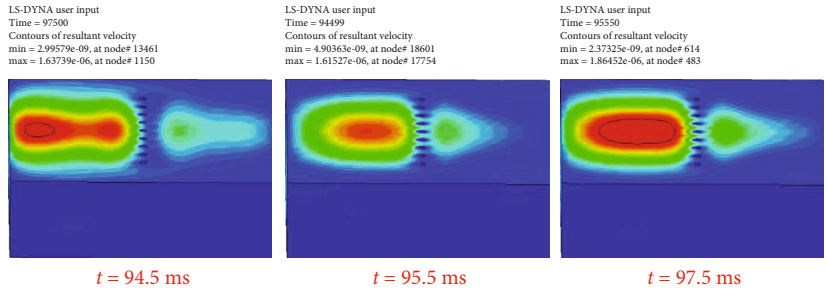

(b) With an artificial free face

Figure 14: Surface velocity cloud images of the vibration (unit: ms).

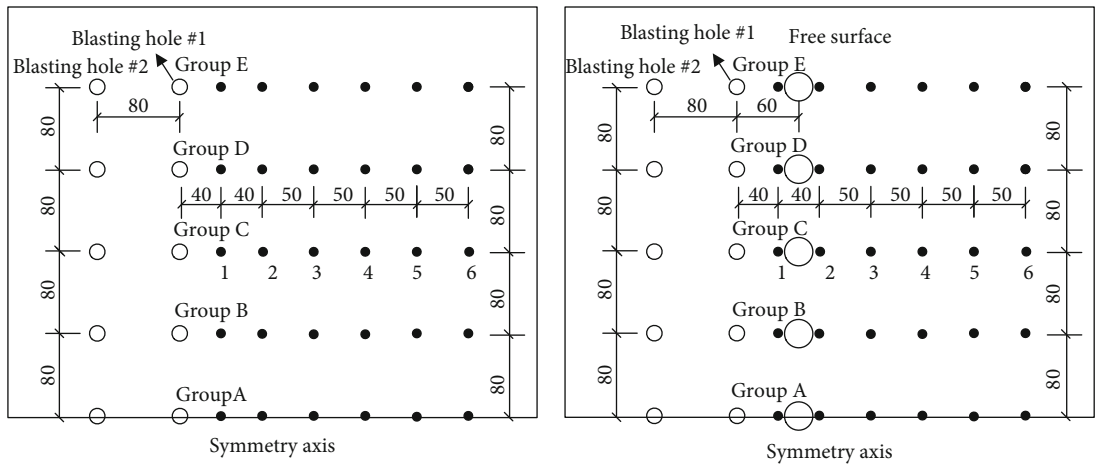

(a) Without an artificial free face

(b) With an artificial free face

Figure 15: Schematic diagram of the selected surface particles.

specific internal energy; A, B, R_1, R_2, and ω are undetermined parameters. According to the actual situation of using explosives onsite, the selected parameters are shown in Table 6.

Under the action of dynamic loads such as impact and explosion, the mechanical properties of rock materials are much more complex than those under static loads, so the material constitutive model is selected as an isotropic bilinear elastoplastic model. The selected parameters according to the previous dynamic loading experimental results of granites are shown in Table 7.

Air, which is also a kind of medium, exists in the artificial empty holes, so the parameters of air in the software need to be defined. In this test, MAT_NULL is used to simulate the air material in the empty holes, and its polynomial state equation is as follows:

$$P = \left(C_0 + C_1\mu + C_2\mu^2 + C_3\mu^3\right) + \left(C_4 + C_5\mu + C_6\mu^2\right)E_0, \quad (3)$$

where $C_0 \sim C_6$ are constants; μ is the volume parameter; E_0 is the ratio of internal energy to initial volume, and the specific parameters are shown in Table 8 as follows:

In order to improve the accuracy of the numerical tests, the elastoplastic model is also used for the analysis and calculation of the constitutive model of the soil layer, and its

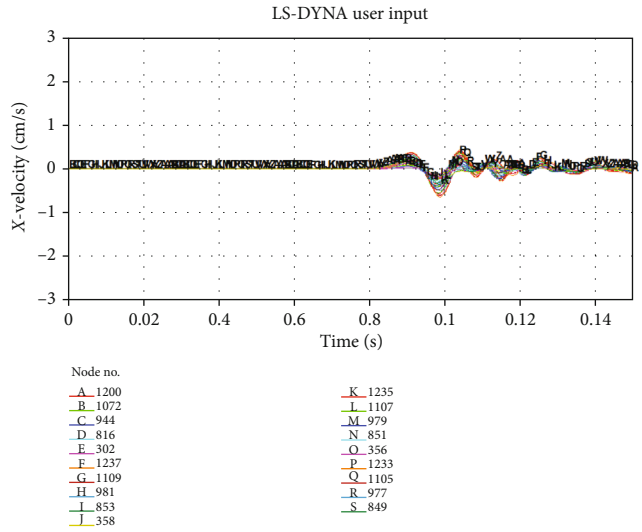

(a) X direction

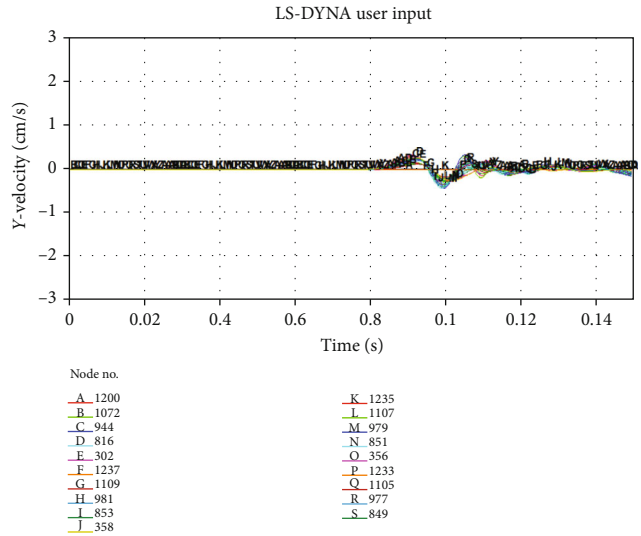

(b) Y direction

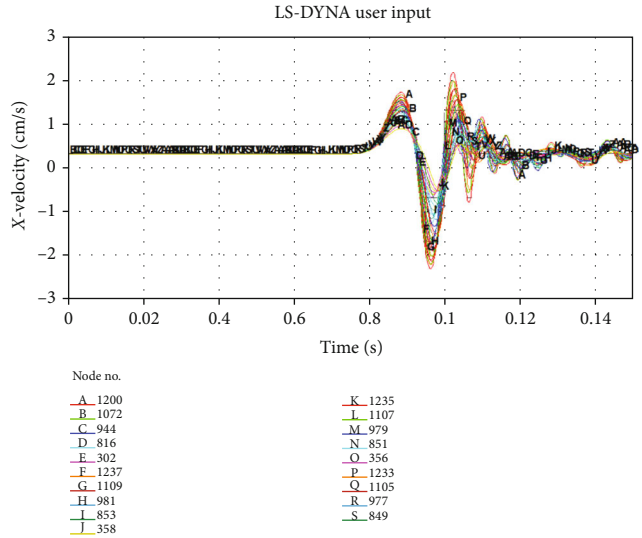

(c) Z direction

Figure 16: Time history curves of three-dimensional vibration velocity of particles.

Table 10: Peak values of the particle vibration velocity in the Z direction.

Free face	Particle no.	Distance from the center of the hole (cm)	Peak vibration velocity of a particle in the Z direction (cm/s)				
			Group A	Group B	Group C	Group D	Group E
With	1	40	1.31	1.16	0.82	0.51	0.32
	2	80	0.65	0.57	0.41	0.26	0.21
	3	130	1.27	1.13	0.81	0.54	0.38
	4	180	1.13	1.01	0.76	0.59	0.46
	5	230	0.86	0.78	0.58	0.5	0.41
	6	280	0.73	0.65	0.47	0.39	0.37
Without	1	40	2.96	2.84	2.48	1.79	1.11
	2	80	2.85	2.73	2.34	1.65	1.03
	3	130	2.76	2.64	2.21	1.55	0.99
	4	180	2.64	2.51	2.05	1.44	0.95
	5	230	2.45	2.31	1.86	1.35	0.94
	6	280	2.2	2.06	1.69	1.27	0.93

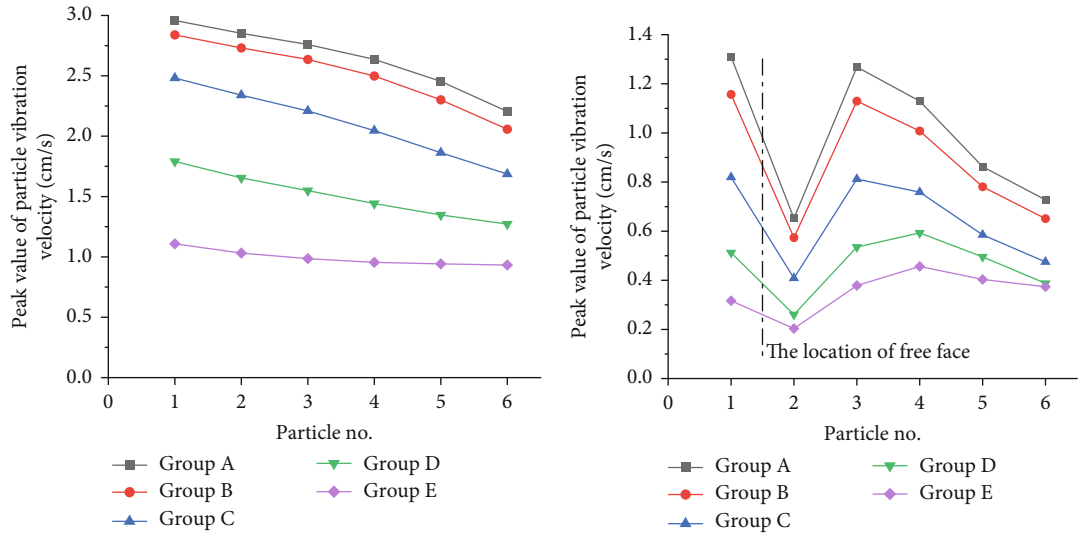

(a) Without an artificial free face

(b) With an artificial free face

Figure 17: The peak vibration velocity curves of particles.

Table 11: Decreasing degree of the peak vibration velocity of particles.

Particle no.	Distance from the center of the hole (cm)	Reduction degree of the peak vibration velocity (%)				
		Group A	Group B	Group C	Group D	Group E
1	40	55.72	59.24	66.97	71.39	71.45
2	80	77.13	79.01	82.54	84.24	80.26
3	130	54.03	57.13	63.25	65.42	61.56
4	180	57.15	59.66	62.92	58.89	52.19
5	230	64.86	66.06	68.61	63.22	57.19
6	280	67.01	68.36	71.84	69.52	59.93

parameters refer to the geological prospecting data of the project, as shown in Table 9.

In blasting construction, each hole needs to be detonated at a certain time interval to ensure good construction effects. Langefors obtained a reasonable time interval formula to improve the crushing effect by analyzing the field measured data, and it is shown as follows:

$$\Delta t = 3.3\,\text{kW}, \tag{4}$$

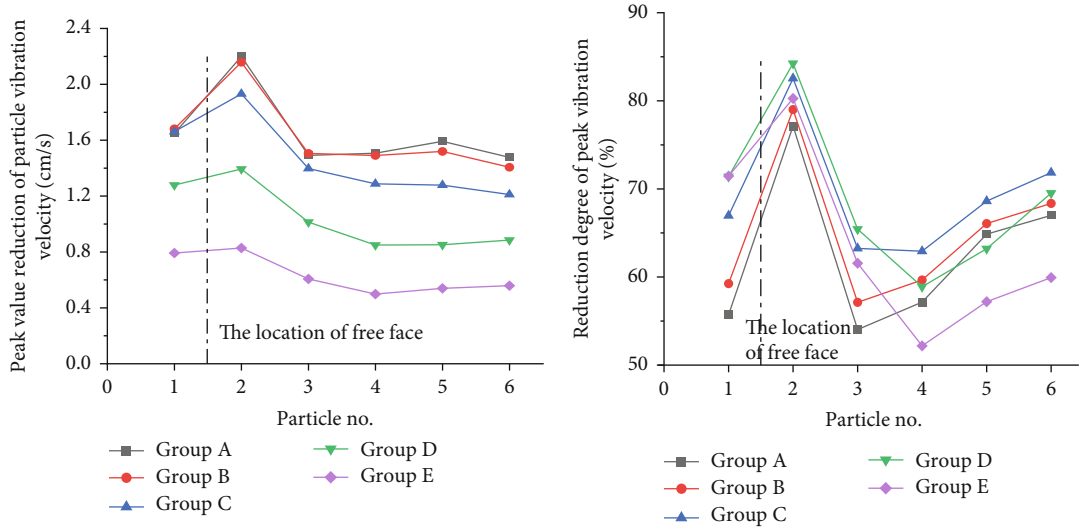

(a) Reduction value of the peak velocity

(b) Reduction degree of the peak velocity

Figure 18: The difference between peak vibration velocities for cases with/without free faces.

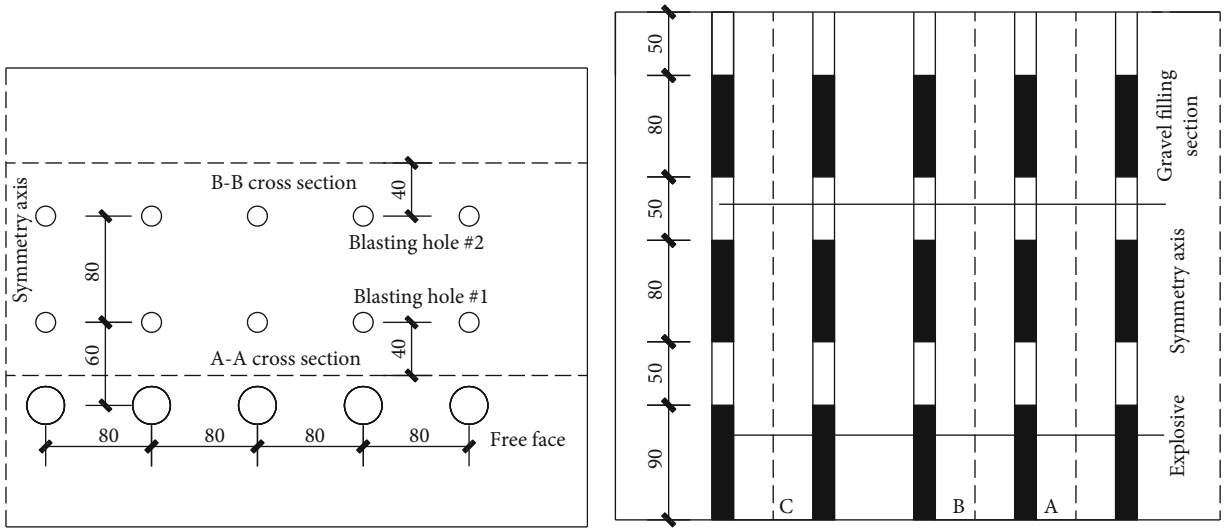

(a)

(b)

Figure 19: Cross section diagram (unit: cm).

where k can be taken as 1 ~ 2, considering the influences of site factors, and W is the minimum resistance line, which equals 0.6 m in this study. From the formula calculation, the time interval is $\Delta t = 1.98 \sim 3.96$ ms, and in the numerical simulation, the time interval of 2 ms is selected.

3.3. Numerical Simulation Results and Analysis. In order to facilitate a comparative analysis, the bedrock part of the numerical model is divided into two parts by taking the artificial free face boundary as the interface, as shown by part 7 and part 9 in Figure 12. Part 7 is the bedrock needed to be treated by blasting, and this is where the explosive is buried.

Figure 13 shows the generation and propagation of explosion stress waves. After the explosive in the first row of holes is detonated, the explosion stress wave propagates outward in the shape approximately similar to a cylinder, and the explosion stress waves formed by each section are superimposed. When $t = 300\ \mu$s, the explosion stress wave propagates to the interface of part 7 and part 9, and there is not much difference between the two models. When the time is larger than 600 μs, it can be seen that in the model with an artificial free face, the explosion stress wave presents a concentrated reflection at the position of the free face. Most explosion stress waves are reflected back to part 7, and only a small part of the explosion stress waves are transmitted to part 9 through the hole and the interval between holes. The action range of the stress waves in part 9 is relatively small, and stress waves decay with a fast speed. The artificial free surface hinders and weakens the propagation of explosion stress waves, and more energy is reflected back to part 7 and continues to act on the bedrock that needs blasting treatment.

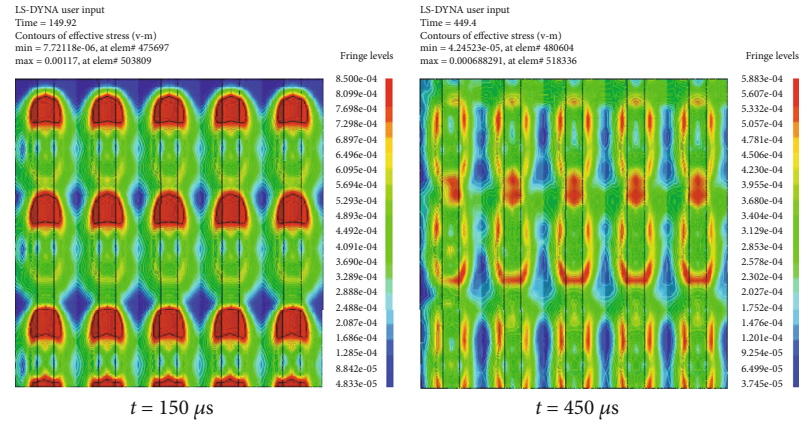

(a) Without a free face

(b) With a free face

Figure 20: Effective stress cloud images of cross section A-A in the bedrock.

In the model without a free surface, there is no concentrated reflection, and the propagation speed of explosion stress waves in part 9 is relatively faster, with a larger action range. It shows that the existence of the artificial free face reflects more explosion stress waves back and continue to act on the bedrock that needs blasting treatment, which improves the utilization rate of explosion energy.

Studies have indicated that there is a good correlation between the vibration response law of building structures and the peak vibration velocity of particles. Therefore, the distribution of a vibration velocity field on the surface is qualitatively analyzed from the surface vibration velocity cloud images. The peak value of the particle vibration velocity is used as the judgment basis of the vibration control.

Figure 14 presents the vibration velocity cloud images of each particle on the surface obtained by the software. After the explosive in the bedrock is detonated, the explosion seismic wave reaches the surface at 94.5 ms, and the vibration intensity reaches its maximum at 95.5 ms. The explosion seismic wave propagates to the two sides from the center of the blasting holes. In the model without an artificial free face, the seismic wave diffusion is more uniform, and the vibration velocity on both sides of the hole is similar, with an axisymmetric distribution. In the model with an artificial free face, it can be found that when the explosion wave propagates towards the free face side, it is hindered by the free face, and only a small part of the blast wave passes through the free face. The vibration velocity on the right side of the free face decreases significantly compared with the model without a free face. Most of the seismic waves are reflected back by the free face, resulting in the vibration velocity on the left side of the artificial face being significantly greater than that on the right side. Therefore, the existence of free faces hinders the propagation of seismic waves and significantly reduces the explosion vibration intensity in the areas that do not need to be blasted.

By recording the peak velocity of the selected surface particles, the weakening effect of the artificial free face on the explosion vibration intensity is quantitatively analyzed. Since the model is symmetric, half of the model is used for analysis. The buildings that need to be protected by the explosion are all on the right side. Six measuring points are taken from the right side, as shown in Figure 15. The horizontal distances between the blasting holes and the measuring points are 40 cm, 80 cm, 130 cm, 180 cm, 230 cm, and 280 cm, respectively, with group A to group E from bottom to top, and point 1 to point 6 from left to right, respectively.

According to the relevant provisions of blasting safety, three components of particle vibration perpendicular to each other should be measured simultaneously during blasting vibration monitoring. The direction of the maximum velocity is the principal vibration direction, and the vibration

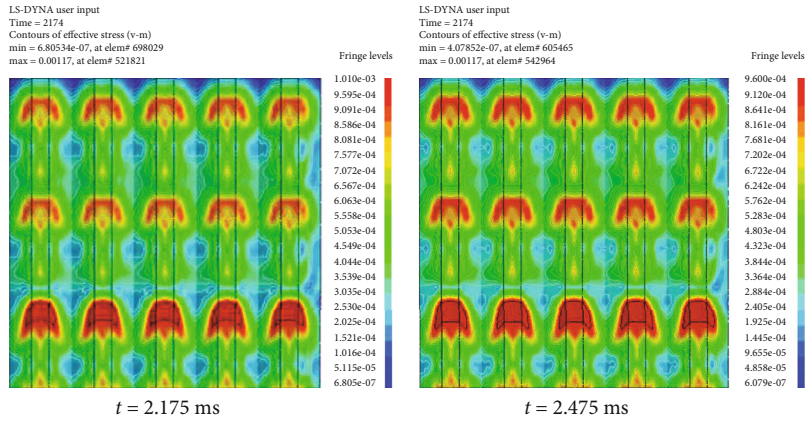

t = 2.175 ms t = 2.475 ms

(a) Without a free face

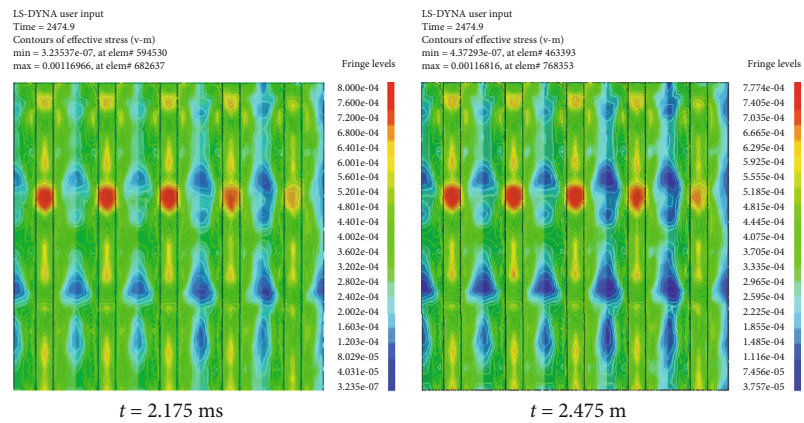

t = 2.175 ms t = 2.475 m

(b) With a free face

Figure 21: Effective stress cloud images of the cross section B-B in the bedrock.

frequency is the principal vibration frequency. The principal vibration velocity and the principal vibration frequency should be considered comprehensively. From the simulation results, it is found that the peak vibration velocity in the Z direction is much larger than that in the X and Y directions (Figure 16); thus, the peak vibration velocity value in the Z direction of the selected particle is mainly analyzed.

From Figure 16, the shapes of the three-dimensional vibration velocity curves of the particles are relatively similar. After the explosive in the bedrock is detonated, the explosion seismic wave is transmitted to the surface at 80 ms, and the surface blasting vibration intensity reaches the maximum at 95 ms, and then gradually decreases. When the time reaches 120 ms, the surface blasting vibration intensity is very small.

The peak vibration velocity of the selected particle in the Z direction is counted, as shown in Table 10, with the variation curves plotted in Figure 17.

From Table 10 and Figure 17, it can be found that the peak vibration velocity at each particle with a free face is lower than that without a free face. The peak value of the particle vibration is 2.96 cm/s without an artificial free face, but it is only 1.31 cm/s with an artificial free face. Obviously, the existence of a free face has a significant effect on reducing the blasting vibration intensity.

For the case without a free face, the peak vibration velocity values of the six points in each group decrease with an increase in distance, and the decreasing range is smaller as the distance is closer to the boundary. The peak vibration velocity values of groups A and B, which are close to the axis of symmetry, are the closest, and are much larger than those of the other groups. This is because at the position of symmetry axis, the explosion effect is more concentrated, but to the direction of both sides, the vibration intensity declines gradually.

For the case with a free face, it can be found that the peak vibration velocity at midpoint #1 of each group is large. As the distance gets further, the peak velocity value decreases, which corresponds to the attenuation phenomenon of seismic waves in the case without a free face. It is worth noting that the peak vibration velocity of the five groups undergoes a sudden drop at point #2, because this point is the first point which is located at the right side of the empty holes and closest to the free face. The existence of the empty holes hinders the propagation of seismic stress waves, causing most of the stress waves to be reflected. It is found that the peak velocity at point #3 climbs significantly, because this is the part of the stress wave which propagates through the interval of the empty holes that causes vibration at point #3.

The reduction degree of the peak vibration velocity of each particle among the cases with/without a free face is calculated and listed in Table 11 and Figure 18.

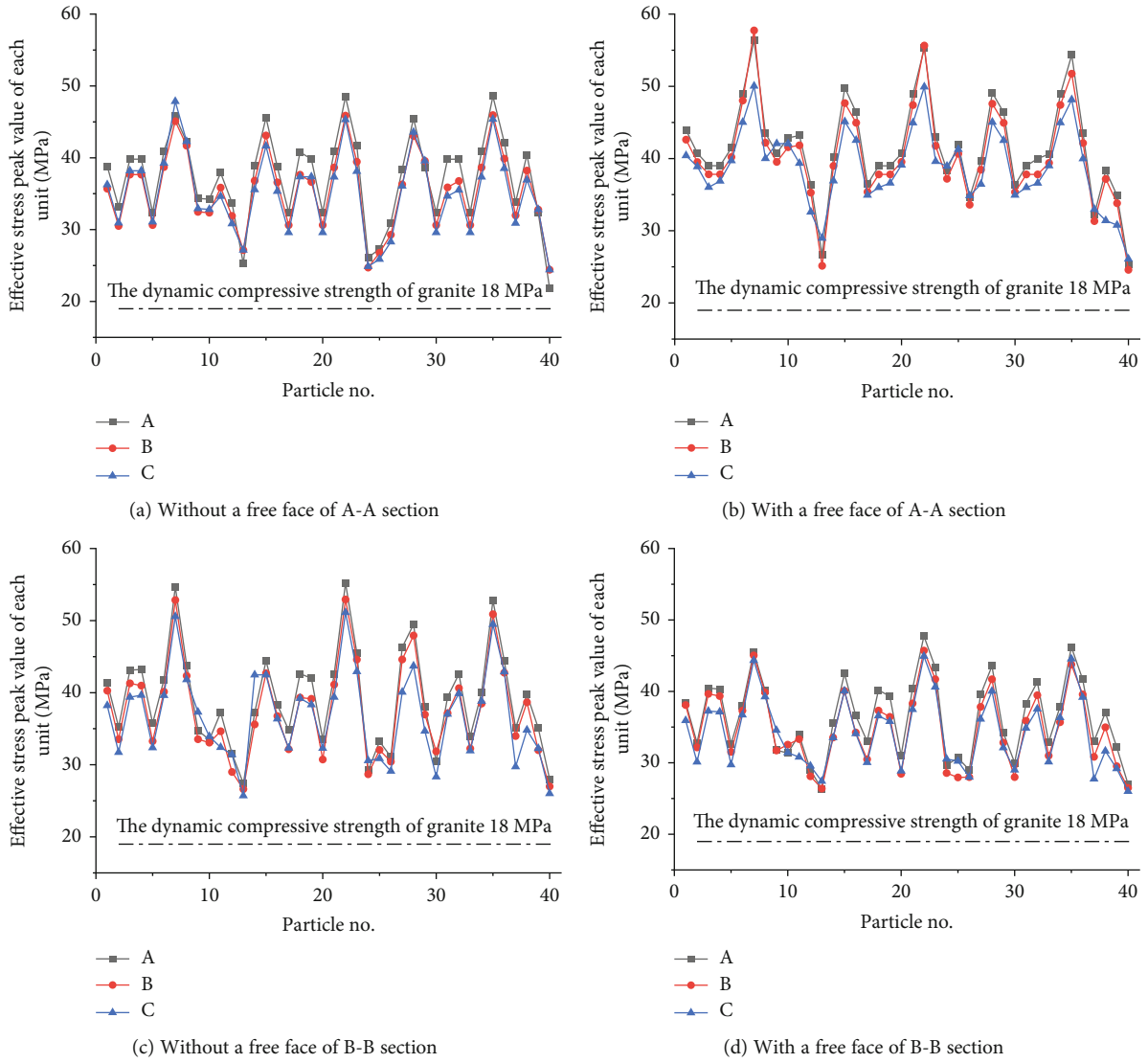

Figure 22: Peak effective stress values of the units.

From Table 11 and Figure 18, the artificial free face has a weakening effect on the peak values of the vibration velocity for each point, and the overall reduction degree is over 55%, among which, the reduction value of point #2 and the corresponding reduction degree are the largest. This is because the position of point #2 is closest to the empty holes at the right side, and an empty hole blocks and reflects most of the seismic stress waves; thus, the peak vibration velocity value of point #2 reduces greatly. With the increase of the distance between the empty holes and the measure points, the peak value reduction of the particle vibration velocity drops down and then stays at a relatively stable level, but the reduction degree of the peak vibration increases gradually; the reason is that the free face hinders the propagation of part of the explosion stress wave, so that the peak value of the latter 4 particles stays at a relatively stable level, while the peak velocity itself decreases with the increase of the distance, thus leading to the increase of the reduction degree.

The stress state of granites under blasting loads is very complicated—it is a three-dimensional stress state of a tension-compression mixture. The Mises yield criterion is selected to analyze the stress state and failure characteristics of granites under an explosion load.

The effective stress at any point in the rock can be expressed as follows:

$$\sigma_e = \frac{1}{\sqrt{2}}\sqrt{(\sigma_1-\sigma_2)^2+(\sigma_1-\sigma_3)^2+(\sigma_2-\sigma_3)^2}. \quad (5)$$

To judge whether rock failure occurs, the following formula is used:

$$\sigma_e \geq \sigma_0. \quad (6)$$

According to the different values of σ_0, the rock has different failure modes:

$$\sigma_0 = \begin{cases} \sigma_{cd}\,(\text{crushing circle}), \\ \sigma_{td}\,(\text{crack circle}), \end{cases} \quad (7)$$

where σ_0 is the uniaxial failure strength, σ_{cd} and σ_{td} are the dynamic uniaxial compressive strength and tensile strength, respectively. The dynamic tensile strength of rock changes little with the loading strain rate; thus, we can take both σ_{td} and σ_t as equal to the tensile strength of rock. The tensile strength of the rock in this study is 18 MPa from the experimental results.

Because the volume of bedrock is too large, it is impossible to measure the effective stress state throughout the bedrock. Therefore, two cross sections (A-A and B-B) are, respectively, selected, as shown in Figure 19(a). Both sections are 40 cm away from the nearest blasting hole. The A-A section is located at one side of the first row of blasting holes and is mainly affected by the explosion of the first row of blasting holes; thus, the effective stress cloud images at 150 μs and 450 μs are selected (Figure 20).

From Figure 20, after the blast of the first row of boreholes, the stress wave is transmitted to the section at 150 ms, and the peak effective stress value reaches the maximum. Afterwards, the peak effective stress value begins to decline. It can be found that the peak stress near the explosive section is higher, while the peak stress near the gravel filling section and the gap area of the blast holes is relatively lower, due to the fact that the closer the blasting area is, the greater the intensity of the explosive stress waves and the greater the effective stress. Compared with the stress cloud images at the same time, the distribution of the effective stress field is roughly similar, while there is a certain difference between the maximum effective stress, with a difference of 4 MPa at 150 ms and a difference of 3 MPa at 450 ms. In the case without a free face, the effective stress value is smaller and the distribution range of the minimum value is larger, which indicate that the free face reflects a part of the stress waves back to the blasting area and enhances the explosion effects.

The B-B section is mainly affected by the second row of holes. The second row of holes is detonated 2 ms after the explosion of the first row of holes. The effective stress cloud maps at 2.175 ms and 2.475 ms are selected, respectively, as shown in Figure 21. The effective stress distribution of the B-B section is relatively similar to that of the A-A section. However, at the same time, it can be seen that the maximum effective stress of the B-B section is larger than that of the A-A section, because the stress waves generated by the second row of explosives overlaps with the stress waves generated by the first row of explosives.

To better analyze the distribution of the peak effective stress of bedrock, three positions of A, B, and C are, respectively, selected on the cross section. A and B are near the symmetry axis, and C is near the boundary, as shown in Figure 19(b). A total of 40 units from the bottom to the top of the bedrock, with a unit spacing of 10 cm, were selected. From the bottom to the top surface, the units were named No. 1~No. 40, respectively. The peak effective stress values of the units were calculated, as shown in Figure 22.

From Figure 22, all of the peak effective stress values of the units exceed the dynamic tensile strength of granites, which lead to the yielding and failing of the units. The peak effective stress for the case with an artificial free face is basically around or above 35 MPa, while the peak value of the case without an artificial free face is concentrated around or above 30 MPa, which is lower than the case with a free face. It has been verified that the free face can reflect a part of the explosion stress waves, which increases the blasting peak stress value and improves the blasting effect. In the area perpendicular to the blasting interval, the effective stress of the unit is relatively larger, while in the area perpendicular to the blockage interval of the blasting holes, the effective stress is relatively small.

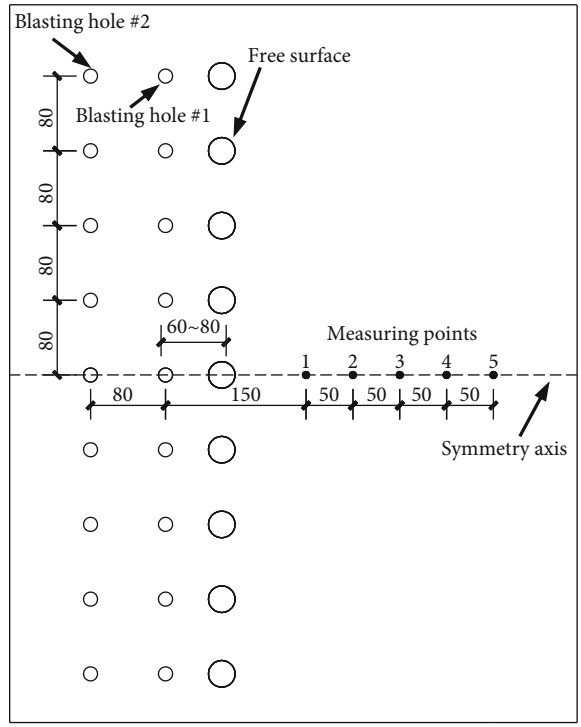

Figure 23: Particle selection diagram on the model surface.

3.4. Parameter Optimization of the Artificial Free Face. The distance between the artificial free face and the center of blasting holes, and the size of the free face are the main factors affecting the effect of the artificial free face. According to construction experience, the row distance between the empty holes and blasting holes should be smaller than the row distance between the blasting holes, and the diameter of the empty holes should be larger than that of the blasting holes. Thus, two factors, including the row distance between empty holes and blasting holes, and the diameter of the empty holes, are selected in the simulation to analyze the influence of different artificial free face parameters on the blasting effects. The row distances are 60 cm, 65 cm, 70 cm, 75 cm, and 80 cm, respectively, and the diameters of the empty holes are 100 mm, 160 mm, 200 mm, 250 mm, and 300 mm, respectively. Five measuring points on the surface are selected to record the data, with the distances from the center of the first row of the blasting holes of 150 cm, 200 cm, 250 cm, 300 cm, and 350 cm, respectively (Figure 23). The peak vibration data in the Z direction of each point are recorded.

Using the postprocessing software LS-PrePost [29], the vibration velocity in the Z direction of each point without

Table 12: Peak values of the vibration velocity in the Z direction without a free surface.

Particle no.	No. 1	No. 2	No. 3	No. 4	No. 5
Peak velocity in the Z direction (cm/s)	2.64	2.45	2.16	2.08	1.89

Table 13: Peak values and average reduction degree of the vibration velocity in the Z direction.

Distance (cm)	Diameter (mm)	Peak vibration velocity of particle in Z direction (cm/s)					$\bar{P}$ (%)
		No. 1	No. 2	No. 3	No. 4	No. 5	
60	100	1.27	0.96	0.88	0.91	1.01	54.8
	160	1.19	0.92	0.78	0.73	0.85	50.2
	200	1.13	0.81	0.63	0.74	0.79	63.2
	250	1.08	0.81	0.61	0.72	0.75	64.7
	300	1.05	0.78	0.59	0.72	0.76	65.2
65	100	1.39	0.98	1.01	0.86	0.95	53.9
	160	1.2	0.87	0.78	0.87	0.85	59.2
	200	1.15	0.88	0.75	0.71	0.76	62.3
	250	1.11	0.86	0.72	0.68	0.72	63.7
	300	1.06	0.88	0.69	0.65	0.71	64.6
70	100	1.54	1.12	0.95	0.95	1.04	50.2
	160	1.29	0.91	0.8	0.85	0.91	57.6
	200	1.18	0.89	0.72	0.79	0.83	60.6
	250	1.13	0.87	0.67	0.67	0.81	63.1
	300	1.09	0.85	0.71	0.66	0.78	63.5
75	100	1.67	1.18	1.08	1.01	1.09	46.4
	160	1.35	0.97	0.96	0.89	0.93	54.6
	200	1.24	0.91	0.76	0.79	0.85	59.5
	250	1.18	0.87	0.69	0.76	0.82	61.6
	300	1.14	0.86	0.72	0.77	0.79	61.9
80	100	1.76	1.18	1.06	1.05	1.08	46.1
	160	1.43	1.05	1.01	0.88	0.85	53.8
	200	1.32	0.94	0.83	0.79	0.77	58.9
	250	1.25	0.94	0.81	0.73	0.69	61.1
	300	1.19	0.91	0.83	0.72	0.68	62.2

and with an artificial free face is obtained. The average reduction degree of the peak stress values of particles is taken as the evaluation index, calculated using equation (8), and the calculated values are summarized in Tables 12 and 13.

$$\bar{P} = \frac{1}{n}\sum_{1}^{n} P_i, \tag{8}$$

where P_i is the reduction degree of the peak vibration velocity for the particle i, and n is the number of measuring points.

From Tables 12 and 13, the peak vibration velocity values of particles in the Z direction with a free face decreases significantly compared with the case without a free face, which is consistent with the previous conclusions. The average reduction degree is basically more than 50%, reflecting that the artificial free face significantly hinders the propagation of explosion stress waves. In order to further quantitatively represent the influence of a free face on the peak vibration velocity of each point, the peak vibration velocity and the reduction degree of peak values are drawn in Figures 24 and 25.

Figures 24 and 25 show that the peak value of particle vibration velocity generally presents a downward trend with the increasing diameter of the empty holes. As the diameter is increased from 100 mm to 200 mm, the curve is relatively steep, and then the downward trend of the curve gradually slows down in the diameter range of 200 mm to 300 mm. The decrease extent of the peak velocity is getting smaller and smaller, with the total decrease amplitude of less than 0.1 cm/s. However, the average decrease degree of the peak velocity shows an opposite trend, indicating a significant increase in the diameter range from 100 mm to 200 mm, and then a gentle increase trend as the diameter increases from 200 mm to 300 mm. This is because with the increase of the hole diameter, the effective area of the free surface will inevitably increase, which will hinder and weaken the stress waves more obviously, leading to the decrease of the particle

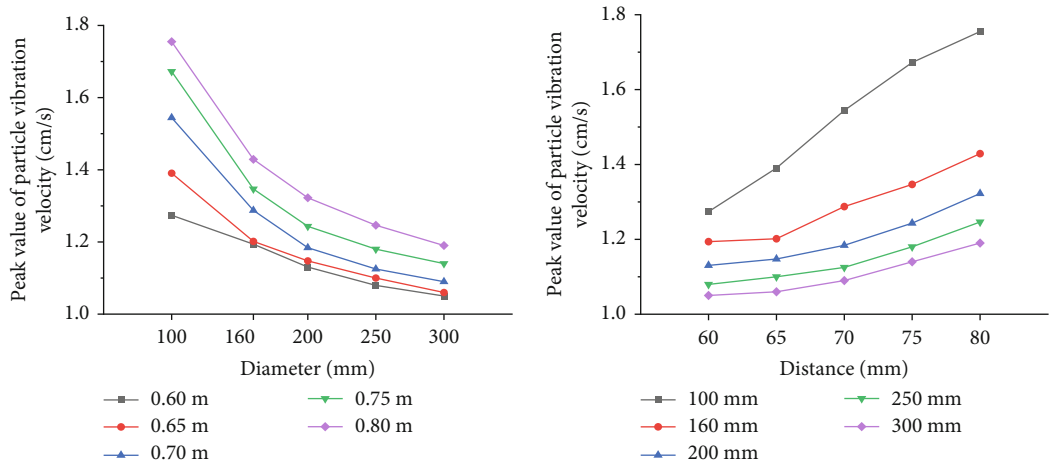

Figure 24: The influence of diameter and distance on the peak value of particle vibration velocity.

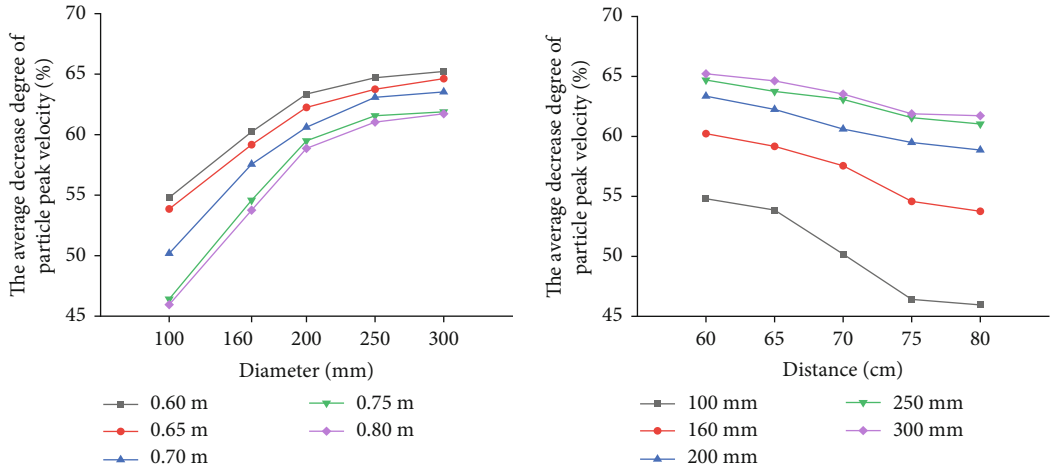

Figure 25: The influence of diameter and distance on the average decrease of peak velocities.

vibration velocity. When the hole diameter increases to a certain extent, the increase extent of the effective area of the free surface will slow down, which will lead to a reduction in the decrease extent of the peak vibration velocity.

When the distance between the artificial free faces and the blasting holes increases from 60 mm to 65 mm, the increase in the peak velocity is relatively small, while the increase extent of the peak velocity is large in the distance range of 65 mm to 80 mm. Variations in the average decrease degree present an opposite trend, which at first declines slowly in the distance range of 60 mm to 65 mm and then declines quickly in the range of 65 mm to 80 mm. This is mainly because when the distance between the artificial free face and the blasting holes is small, the energy carried by the explosion stress waves from the blasting holes to the free surface is correspondingly high. The artificial free face has a strong blocking and weakening effect on the explosion stress wave. However, when the distance between the free face and the blast holes is large, a considerable part of the explosion stress wave propagates around the free face. Therefore, the control effect on the blasting vibration intensity will be reduced to a certain extent.

The free face has a significant effect on the obstruction of the explosion stress waves, with an average reduction degree of 50% or more, which can greatly reduce the peak vibration velocity and play a protective role for the buildings. The larger the hole diameter, the better the blocking effect will be. However, considering the labor cost and the obtained blocking effect, 200 mm is the best diameter of the hole, and 60 cm is the best distance between the artificial free face and the blasting holes.

4. Conclusions

Through the numerical simulation method, the principle and influence of the artificial free face that hinder the propagation of explosive stress waves were explored. Two groups, one with artificial free faces and the other without, were set for comparison tests, and the effective stress on the bedrock and the peak vibration velocity of the measuring points were studied. Based on the numerical results, the influences of the diameter of the empty holes and distance between the empty holes to the blasting holes on the blasting effects of the bedrock were studied. The parameter optimization of the

artificial free surfaces in rock blasting are carried out. The main conclusions are drawn as follows:

(1) Under an applied axial load, the granites are characterized by a typical splitting failure mode with tensile cracks along the loading direction. The average UCS, axial failure strain, secant Young's modulus, tangent elasticity modulus, and Poisson's ratio are 114.01 MPa, 0.0055, 18959.6 MPa, 24713.3 MPa, and 0.26, respectively. The dynamic peak compressive strength increases with the increasing strain rate. With an increasing excitation pressure, the number of fragments increases, and the failure degree increases gradually

(2) Due to the reflection effect of the artificial free face, it can control the vibration intensity of the surface, and the reduction degree of the peak velocity of the surface particle can reach more than 50% and the reduction degree of the peak velocity of the particle near the artificial free face can reach more than 77%

(3) The distribution of the effective stress field in the bedrock has a close relationship with the charging structure. The peak value of the effective stress near the charge area is larger than that near the gravel blockage area. The existence of the artificial free face makes the stress wave reflect and superimpose with the original stress waves, increasing the effective stress in the blasting area, and the effective stress can be increased by 5 MPa or more

(4) The increase of the diameter of the empty holes can decrease the peak vibration velocity of the surface particle and improve the blasting effect. When the diameter of empty holes is 200 mm and 250 mm, the control effect is the most significant. The increase of the distance between the empty holes and the blasting holes can cause the decrease of the control effect

(5) Based on the comprehensive consideration of blasting effects and construction cost, the parameter design value of the artificial free face is put forward, the diameter of the hole is 200 mm, the distance between the empty holes and the center of the blasting holes is 60 cm, and the depth of the empty hole is the same as the blasting hole. Two rows of blasting holes and one row of empty holes are adopted in the construction condition, and the artificial free face is located on the side of the building structure that needs to be protected

Data Availability

All data used during this study are available from the corresponding author by request.

Conflicts of Interest

The authors declare that they have no known conflicts of interests or personal relationships that could have appeared to influence the work reported in this paper.

Acknowledgments

The authors gratefully acknowledge the financial support from the National Natural Science Foundation of China (Nos. 51874292 and 51934007), the National Key Basic Research and Development Program of China (No. 2016YFC0801403), the Key Basic Research and Development Program of Jiangsu Province (No. BE2015040), and the Innovative Training Program for College Students of China University of Mining and Technology (No. 20200102cx).

References

[1] Q. Wang and X. Yang, "Urbanization impact on residential energy consumption in China: the roles of income, urbanization level, and urban density," *Environmental Science and Pollution Research International*, vol. 26, no. 4, pp. 3542–3555, 2019.

[2] J. Wu, H. Jing, Q. Yin, L. Yu, B. Meng, and S. Li, "Strength prediction model considering material, ultrasonic and stress of cemented waste rock backfill for recycling gangue," *Journal of Cleaner Production*, vol. 276, p. 123189, 2020.

[3] R. Xu, X. Li, W. Yang, M. Rabiei, C. Yan, and S. Xue, "Field measurement and research on environmental vibration due to subway systems: a case study in eastern China," *Sustainability*, vol. 11, no. 23, pp. 1–12, 2019.

[4] H. B. Amnieh, M. S. Zamzam, and M. R. Mozdianfard, "Geological hazards analysis in urban tunneling by epb machine (case study: Tehran subway line 7 tunnel)," *International Journal of Mining and Geo-Engineering*, vol. 50, pp. 1–12, 2016.

[5] Q. Yin, R. Liu, H. Jing, H. Su, L. Yu, and L. He, "Experimental study of nonlinear flow behaviors through fractured rock samples after high-temperature exposure," *Rock Mechanics and Rock Engineering*, vol. 52, no. 9, pp. 2963–2983, 2019.

[6] J. Lv, X. Li, Z. Li, and H. Fu, "Numerical simulations of construction of shield tunnel with small clearance to adjacent tunnel without and with isolation pile reinforcement," *KSCE Journal of Civil Engineering*, vol. 24, no. 1, pp. 295–309, 2020.

[7] R. Coish, J. Kim, N. Morris, and D. Johnson, "Late stage rifting of the Laurentian continent: evidence from the geochemistry of greenstone and amphibolite in the Central Vermont Appalachians 1," *Canadian Journal of Earth Sciences*, vol. 49, no. 49, pp. 232-233, 2012.

[8] J. Sun, P. Zhang, Y. Meng, Z. Li, Q. Wang, and C. Zeng, "Gray relational analysis on parameter sensitivity of blasting rock mass in soft-hard composite strata," *Highway*, vol. 6, pp. 314–318, 2018.

[9] J. Wu, M. Feng, X. Mao et al., "Particle size distribution of aggregate effects on mechanical and structural properties of cemented rockfill: experiments and modeling," *Construction and Building Materials*, vol. 193, pp. 295–311, 2018.

[10] J. H. Yang, W. B. Lu, Q. H. Jiang, C. Yao, and C. B. Zhou, "Frequency comparison of blast-induced vibration per delay for the full-face millisecond delay blasting in underground opening excavation," *Tunnelling and Underground Space Technology*, vol. 51, pp. 189–201, 2016.

[11] Q. Yin, G. Ma, H. Jing, H. Su, Y. Wang, and R. Liu, "Hydraulic properties of 3D rough-walled fractures during shearing: an experimental study," *Journal of Hydrology*, vol. 2017, no. 555, pp. 169–184, 2017.

[12] M. Khandelwal and T. N. Singh, "Prediction of blast induced ground vibrations and frequency in opencast mine: a neural network approach," *Journal of Sound and Vibration*, vol. 289, no. 4-5, pp. 711–725, 2006.

[13] R. Kumar and K. Bhargava, "Determination of blast-induced ground vibration equations for rocks using mechanical and geological properties," *Journal of Rock Mechanics and Geotechnical Engineering*, vol. 8, no. 3, pp. 341–349, 2016.

[14] R. Nateghi, "Prediction of ground vibration level induced by blasting at different rock units," *International Journal of Rock Mechanics and Mining Sciences*, vol. 48, no. 6, pp. 899–908, 2011.

[15] Z. Wang, C. Fang, Y. Chen, and W. Cheng, "A comparative study of delay time identification by vibration energy analysis in millisecond blasting," *International Journal of Rock Mechanics and Mining Sciences*, vol. 60, pp. 389–400, 2013.

[16] H. Li, X. Xia, J. Li, J. Zhao, B. Liu, and Y. Liu, "Rock damage control in bedrock blasting excavation for a nuclear power plant," *International Journal of Rock Mechanics and Mining Sciences*, vol. 48, no. 2, pp. 210–218, 2011.

[17] P. K. Singh, "Blast vibration damage to underground coal mines from adjacent open-pit blasting," *International Journal of Rock Mechanics & Mining Sciences*, vol. 39, no. 8, pp. 959–973, 2002.

[18] J. S. Lee, S. K. Ahn, and M. Sagong, "Attenuation of blast vibration in tunneling using a pre-cut discontinuity," *Tunnelling and Underground Space Technology*, vol. 52, pp. 30–37, 2016.

[19] W. Lu, Z. Leng, H. Hu, M. Chen, and G. Wang, "Experimental and numerical investigation of the effect of blast-generated free surfaces on blasting vibration," *European Journal of Environmental and Civil Engineering*, vol. 22, no. 11, pp. 1374–1398, 2018.

[20] X. Qiu, X. Shi, Y. Gou, J. Zhou, H. Chen, and X. Huo, "Short-delay blasting with single free surface: results of experimental tests," *Tunnelling & Underground Space Technology*, vol. 74, pp. 119–130, 2018.

[21] B. Mohanty, "Explosion generated fractures in rock and rock-like materials," *Engineering Fracture Mechanics*, vol. 35, no. 4-5, pp. 889–898, 1990.

[22] Z. Yue, S. Tian, and Z. Chen, "Influence of the interval between holes on crack propagation in slit charge blasting," *Chinese Journal of Rock Mechanics and Engineering*, vol. 37, no. 11, pp. 2460–2467, 2018.

[23] W. Yuan, X. Su, W. Wang, L. Wen, and J. Chang, "Numerical study of the contributions of shock wave and detonation gas to crack generation in deep rock without free surfaces," *Journal of Petroleum Science and Engineering*, vol. 177, no. 2, pp. 699–710, 2019.

[24] P. Rai, H. S. Yang, and B. S. Choudhary, "Formation of slot cut for creating free face in solid limestone bench: a case study," *Powder Technology*, vol. 228, pp. 327–333, 2012.

[25] J. Tian and F. Qu, "Model experiment of rock blasting with single borehole and double free-surface," *Mining Science and Technology (China)*, vol. 3, pp. 395–398, 2009.

[26] D. Hagan, "The importance of the shape, orientation and roughness of free faces in commercial blasting operations," *Cerebrovascular Diseases*, vol. 24, s1, pp. 181–188, 2007.

[27] D. Johansson and F. Ouchterlony, "Shock wave interactions in rock blasting: the use of short delays to improve fragmentation in model-scale," *Rock Mechanics and Rock Engineering*, vol. 46, no. 1, pp. 1–18, 2013.

[28] G. F. Brent, G. E. Smith, and G. N. Lye, "Studies on the effect of burden on blast damage and the implementation of new blasting practices to improve productivity at KCGMs Fimiston Mine," *Fragblast*, vol. 6, no. 2, pp. 189–206, 2002.

[29] S. S. Aini, B. B. Sahari, A. Ali, A. A. Nuraini, A. A. Faieza, and T. T. Ismail, "Introducing fatigue contour plot in LS-Pre Post LSDYNA finite element crash simulation software," *Applied Mechanics & Materials*, vol. 165, pp. 275–279, 2012.